



Room-Temperature Quantum Cloning Machine with Full Coherent Phase Control in Nanodiamond

Yan-Chun Chang, Gang-Qin Liu, Dong-Qi Liu, Heng Fan & Xin-Yu Pan

Beijing National Laboratory for Condensed Matter Physics, Institute of Physics, Chinese Academy of Sciences, Beijing 100190, China.

SUBJECT AREAS:

QUANTUM
INFORMATION

QUANTUM MECHANICS

QUANTUM OPTICS

OTHER NANOTECHNOLOGY

Received
30 October 2012

Accepted
5 March 2013

Published
20 March 2013

Correspondence and requests for materials should be addressed to H.F. (hfan@iphy.ac.cn) or X.-Y.P. (xypan@aphy.iphy.ac.cn)

In contrast to the classical world, an unknown quantum state cannot be cloned ideally, as stated by the no-cloning theorem. However, it is expected that approximate or probabilistic quantum cloning will be necessary for different applications, and thus various quantum cloning machines have been designed. Phase quantum cloning is of particular interest because it can be used to attack the Bennett-Brassard 1984 (BB84) states used in quantum key distribution for secure communications. Here, we report the first room-temperature implementation of quantum phase cloning with a controllable phase in a solid-state system: the nitrogen-vacancy centre of a nanodiamond. The phase cloner works well for all qubits located on the equator of the Bloch sphere. The phase is controlled and can be measured with high accuracy, and the experimental results are consistent with theoretical expectations. This experiment provides a basis for phase-controllable quantum information devices.

The no-cloning theorem^{1,2} is fundamental in quantum mechanics and quantum information processing. To clone quantum states, various quantum cloning machines, which can clone quantum states either approximately^{3–8} or probabilistically⁹, have been proposed and implemented in different physical systems^{10–12}, see two reviews^{13,14}. In addition to exploring the capabilities of cloning processes in the quantum world, one direct application of quantum cloning is its role in analysing the security of quantum key distributions (QKDs), which are secure under all conditions because of the no-cloning theorem. The well-accepted Bennett-Brassard 1984 (BB84) quantum key distribution protocol¹⁵ uses four quantum states: to transmit information through a public quantum channel so that secure keys can be generated. A quantum strategy that can be adopted by an eavesdropper is to quantum clone the transmitted BB84 states. Quantum cloning the BB84 states is equivalent to cloning the four states $(|0\rangle + e^{i\varphi}|1\rangle)/\sqrt{2}$, where $\varphi = j\pi/2$, $j = 0, 1, 2, 3$, which we also refer to as BB84 states in this work. Note that all four of these states are located on the equator of the Bloch sphere.

In the general quantum cloning process, a unitary transformation acts on a system composed of the BB84 input states, the blank state and the ancillary state, to obtain two optimal output copies. The general form can be written as $U|00R\rangle = a|00A\rangle + b|01B\rangle + c|10C\rangle + d|11D\rangle$, $U|10R\rangle = e|00E\rangle + f|01F\rangle + g|10G\rangle + h|11H\rangle$. Because the BB84 states are used randomly, an attack by quantum cloning should be symmetric in those four states. In general, we use the fidelity between the input state and the output copies to quantify the similarities between the input state and the output copies, which can be used as a measure of quality for a cloning machine. If two copies are equivalent, optimal cloning of the BB84 states is realised by the transformations $|00\rangle \rightarrow |00\rangle$ and $|10\rangle \rightarrow (|01\rangle + |10\rangle)/\sqrt{2}$. Here, the ancillary state is not necessarily needed; elimination of the ancillary state can conserve limited qubit resources. The corresponding optimal fidelity is $F = \frac{1}{2} + \frac{1}{\sqrt{8}}$. Interestingly, we note that both the cloning transformations and the fidelity presented above are optimal if we clone all qubits located on the equator of the Bloch sphere with the form $(|0\rangle + e^{i\varphi}|1\rangle)/\sqrt{2}$; here, the phase φ is arbitrary^{7,16–18}. Thus, the phase quantum cloning machine is optimal for cloning BB84 states; i.e., the phase quantum cloning machine is equivalent to the optimal cloning machine for BB84 states.

For the previous experiment in a solid-state system¹⁹, only two different phases were precisely prepared, and only a fixed phase parameter was measured. The arbitrary phase was realised through free time evolution. In this article, all of the different phases in our reported experiment are precisely prepared and controlled; this approach ensures that the phase cloning machine is successfully implemented, and the measurement is performed by standard state tomography, which is easier to implement. Our experiment is implemented in the nitrogen-vacancy (NV) defect centre of diamond at room temperature. This solid-state system is one of the most promising



candidates for quantum information processing (QIP)^{20,21}. Many coherent control and manipulation processes have been performed with this system^{22–34}. It is more challenging to implement the experiment in nanodiamond than in a bulk sample because of the coherence time. However, nanodiamond shows more potential for further integration and applications. Compared with a bulk sample, the NV centre in nanodiamond has many outstanding characteristics. Because the NV centre in a nanodiamond is sub-wavelength in size, reflection effects at the surface are avoided; thus, the fluorescence collection efficiency is much higher in nanodiamonds than in bulk materials³⁵. In addition, with the aid of microfabrication techniques, the NV centres in nanodiamond can be manipulated and coupled to other systems, such as nanowires^{36,37}, photonic crystals³⁸, waveguides^{39,40}, microspheres⁴¹ and optical fibres⁴². As a result, nanodiamonds play an important role in many applications, such as nanoscale imaging magnetometry, in which a nanodiamond is attached to an atomic force microscope (AFM) tip to measure the magnetic field^{27,43}. The use of nanodiamonds has been demonstrated in plasmon-enhanced single photon emission through the assembly of individual nanodiamonds and gold nanoparticles⁴⁴. Fluorescent nanodiamonds also offer many advantages in biophysics because of their brightness, photostability and biocompatibility⁴⁵.

Results

Experimental system. Our experiment is performed in a nanodiamond sample, and an AFM scanning image of the sample is shown in Figure 1(a). The bright spots are nanocrystals with an average diameter of approximately 50 nm. The laser scanning image of the NV centre investigated is shown in Figure 1(b). The typical fluorescence intensity of nanodiamond is 10^5 counts/s, which is approximately twice that of the bulk sample. Nanodiamond has many advantages but also poses new challenges for coherent control. The NV centre in nanodiamond typically has a short dephasing time, which is caused by the complex spin environment

(rather than the ^{13}C spin bath in a bulk sample)⁴⁶. The typical T_2^* of the NV centre in nanodiamond is only hundreds of ns; Figure 1(c) shows the Ramsey signal of the investigated NV with $T_2^* \sim 700$ ns. Thus, high-speed manipulation of the electron spin state is crucial for applications of the spin state to QIP, especially in complex systems with large microwave losses. In our experiment, a carefully calibrated coplanar waveguide (CPW) antenna is employed to deliver the microwave (MW) pulse to the sample [Fig. 1(b) inset]. The nanodiamonds are spin-coated on a CPW with a quartz substrate. The driven Rabi oscillation frequency reaches more than 50 MHz, which corresponds to a period of 20 ns. This duration is far shorter than the dephasing time of most NV centres in nanodiamonds. Thus, more state manipulations can be implemented before decoherence, Figure 1(c).

The energy level structure of the electron spin of the NV is shown in Figure 1(d) with the corresponding optically detected magnetic resonance (ODMR) spectra. Levels $m_s = +1$ and $m_s = -1$ are split by approximately 250 MHz via an external magnetic field. The quantum states corresponding to $m_s = 0$, $m_s = +1$ and $m_s = -1$ are denoted by $|0\rangle$, $|+1\rangle$ and $|−1\rangle$. Laser and microwave pulses are used to manipulate the electron spin of the NV. Two types of microwave frequencies are used in the experiment: MW1 and MW2. The MW1 frequency is resonant with the transition $|0\rangle \leftrightarrow |+1\rangle$, and MW2 is resonant with $|0\rangle \leftrightarrow |−1\rangle$. The MW1 signal is split into two parts: MW1-P and MW1-M, for state preparation and measurement, respectively. See the Methods section for more information about the experimental system.

Experimental implementation. The implementation of this phase cloning machine includes preparation of the BB84 states, the cloning process and readout of the output. Three energy levels of the electron spin of the NV are used to implement this scheme. The logical BB84 states are encoded by physical spin states as follows: $|+1\rangle \sim |00\rangle_p$, $|0\rangle \sim |10\rangle_l$ and $|−1\rangle \sim |01\rangle_l$ ¹⁹. The electron spin state of the NV can

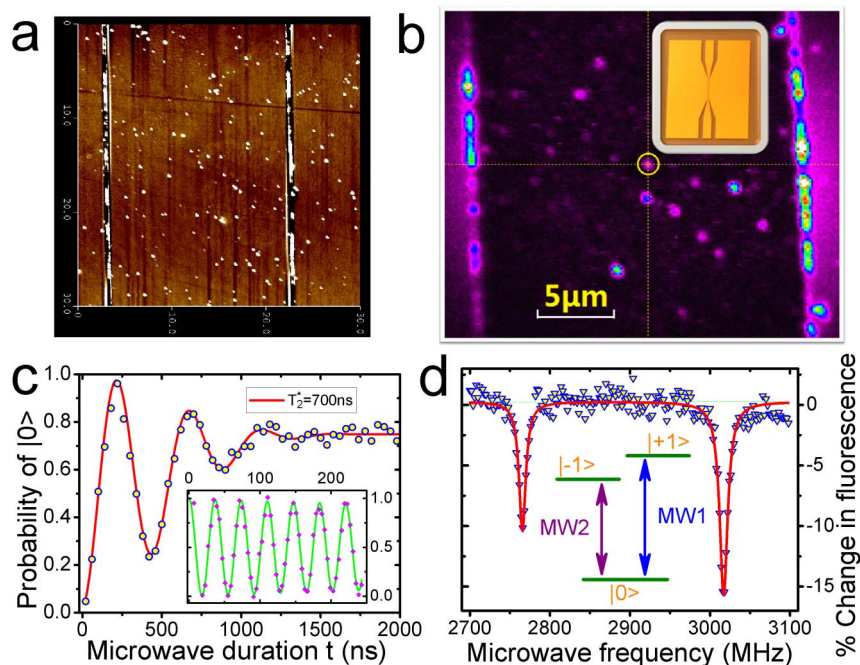


Figure 1 | Nanodiamond samples and the energy level structure of the NV centre. a. AFM scanning image ($30 \mu\text{m} \times 30 \mu\text{m}$) of the nanodiamond samples on CPW. The bright spots are nanocrystals, and the two straight bands are the metal edges of the CPW. b. The NV centre investigated is shown as a bright spot marked with a circle in the two-dimension laser scanning image, in which the CPW margins are also visible. The inset shows the CPW antenna fabricated on a quartz substrate. c. Typical Ramsey signal showing that T_2^* of the NV is approximately 700 ns. With high-frequency Rabi oscillations (inset), more manipulations can be implemented before decoherence. d. The three energy levels involved in the experiment and their corresponding ODMR spectra.



be polarised through laser excitation and can be read from the fluorescence intensity. A microwave pulse with duration $\theta = 2\pi t/T$ (where t is the MW period and T is the Rabi period) can rotate the electron spin by an angle θ , around an axis in the equatorial plane of the Bloch sphere. The angle between the axis of rotation and the x -axis is determined by the phase of the microwave pulse. Thus, a superposition state $|\psi\rangle = \cos\frac{\theta}{2}|0\rangle + e^{i\varphi}\sin\frac{\theta}{2}|1\rangle$ can be prepared with a MW pulse of duration θ and phase φ , Figure 2(c).

As a result, the experiment can be performed by following the control sequence shown in Figure 2(a). First, the electron spin is polarised into state $|0\rangle$ with a 3- μ s laser pulse. A MW1-P pulse with a duration of $\pi/2$ prepares the superposition state $(|0\rangle + e^{i\varphi}|1\rangle)/\sqrt{2}$, where the variable φ is determined by the phase of MW1-P. This step combines the preparation of the input state for the first qubit and the initialisation of the blank state of the second qubit for the logical qubits. We note that the prepared input state actually corresponds to the form $(|1\rangle + e^{i\varphi}|0\rangle)/\sqrt{2}$ for the logical qubit; this form is equivalent to the normal form $(|0\rangle + e^{i\varphi}|1\rangle)/\sqrt{2}$ when φ ranges over all four values in the experiment. In the cloning process, an input state $(|0\rangle + e^{i\varphi}|1\rangle)/\sqrt{2}$ is transferred into an output state $\frac{1}{2}|0\rangle + \frac{1}{2}|1\rangle + \frac{1}{\sqrt{2}}e^{i\varphi}|1\rangle$ by a MW2 pulse with a duration of $\pi/2$. To measure the state phase and probability, a MW1-M or MW2 pulse of variable duration is applied to induce Rabi oscillations

between $|0\rangle \leftrightarrow |1\rangle$ or $|0\rangle \leftrightarrow |-1\rangle$, see the Methods section and Figure 2(d) for details. Finally, the spin state is read by photon counting under pulsed laser excitation. The readout signal is followed by a reference. The entire process is repeated to obtain the statistics of the measurements.

Phase control and measurement. The accuracy of the control of the microwave phase and the measurement of the state phase is verified before cloning. Two mechanical phase shifters, with an adjustment range of $180^\circ/\text{GHz}$, are used to control the microwave phase. In addition to the readings from the phase shifters, the relative phase difference between the two microwaves can be estimated with an in-house designed device to measure microwave phase differences. A motor-driven phase shifter controlled by a computer modulates the MW1-M signal. During the experiment, the shifter automatically switches between two specific positions (X and Y). There is a 90° phase difference between microwaves at these positions of the shifter. The corresponding microwave phases are denoted Phase X (0°) and Phase Y (90°), which provide references for all of the following state phase measurements.

The other phase shifter is manually controlled to modulate the MW1-P signal. Microwaves with various phases can be obtained by adjusting the manual phase shifter. Because a quantum state with a specific phase can be prepared using a microwave pulse with a consistent phase, three states with different phases are tested first. These

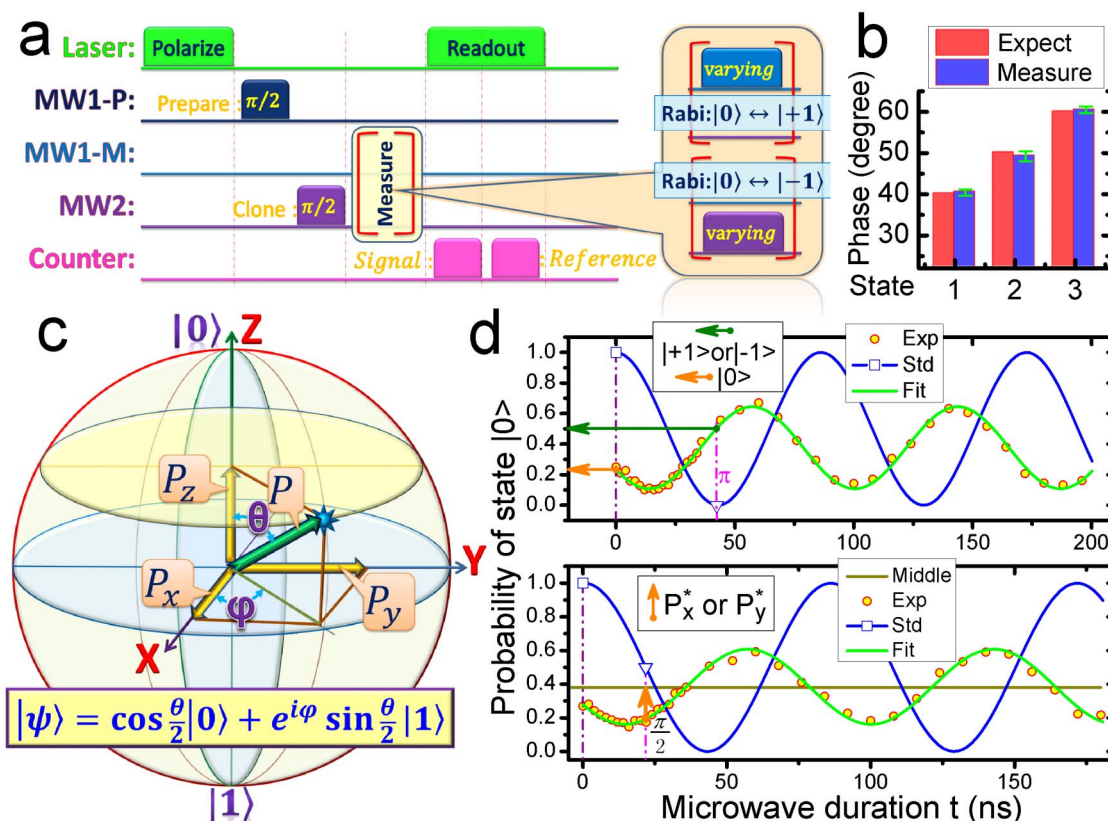


Figure 2 | Scheme for quantum phase cloning. a. Control sequence for the laser, microwave pulses and photon counter. After polarisation with the laser pulse, a $\pi/2$ MW1-P pulse prepares the input state. The quantum cloning process is performed by a $\pi/2$ MW2 pulse. MW1-M or MW2 pulses of various durations are used to implement the Rabi oscillations for the measurement. b. Phase measurement for three test states. The blue columns show the experimental results, and the red columns display the expectation values. The error bars are the standard deviations from seven measurements. c. Bloch sphere representation of the superposition state $|\psi\rangle = \cos\frac{\theta}{2}|0\rangle + e^{i\varphi}\sin\frac{\theta}{2}|1\rangle$ and the Bloch vector P and its X, Y and Z components P_x , P_y and P_z . d. Rabi oscillations are used for the measurement. The blue lines are the standard Rabi oscillations, which are used for scaling. The scatter points show the experimental data, and the green lines represent the fitting results. The upper panel shows the probability measurements. The orange arrow indicates the probability of $|0\rangle$, and the green arrow indicates the probability of $|-1\rangle$ (Rabi C) or $|+1\rangle$ (Rabi S). The lower panel shows the phase measurements. The dark yellow line denotes the middle of the Rabi X or Rabi Y oscillations. The orange arrow indicates the relative distance corresponding to the observation of P_x^* or P_y^* .



state phases are measured over two full Rabi oscillations by MW1-M with X and Y phases; see the Methods section and the lower panel of Figure 2(d) for details. The experimental values are $40.4^\circ \pm 0.8^\circ$, $49.2^\circ \pm 1.2^\circ$ and $60.5^\circ \pm 0.8^\circ$ (standard deviation of seven measurements), whereas the expected values are 40° , 50° and 60° , Figure 2(b). These results demonstrate the high accuracy of the control and the measurement; the small standard deviations also show good phase stability for repetition at long times.

Experimental results. The cloning experiment is implemented with four different input states that are distributed uniformly on the equator of the Bloch sphere, see Figure 3. Coincidentally, these states can serve as BB84 states in QKD.

First, an input state Φ_1 of the form $(|0\rangle + e^{i\varphi}|1\rangle) / \sqrt{2}$ is prepared with the polarisation laser and a $\pi/2$ MW1-P pulse. The state phase is measured five times, and the experimental data points are shown as empty green squares in Figure 3. The average phase before cloning, 44.6° , is shown by the blue line with solid triangles. The standard deviation of the five measurements is $\pm 2.4^\circ$. In the subsequent cloning stage, the input state is converted into the $\frac{1}{2}|0\rangle + \frac{1}{2}|1\rangle + \frac{1}{\sqrt{2}}e^{i\varphi}|+1\rangle$ state with a $\pi/2$ MW2 pulse. The phase measurement results for the output state are shown as empty red circles. The average phase after cloning, 50.4° , is represented by the magenta line with solid triangles, and the standard deviation is $\pm 1.9^\circ$. The phase change for the cloning process is 5.8° ; this change is a reasonable value based on the magnitude of the deviation in the measurement. Thus, the phase information is well preserved during the cloning process.

To confirm the cloning fidelity, we are concerned with not only the state phase but also the probabilities of $|0\rangle$, $|+1\rangle$ and $|-1\rangle$. The probability measurement is also performed five times; the detailed process is described in the Methods section and shown in the upper panel of Figure 2(d). The probabilities of $|0\rangle$ and $|+1\rangle$ can be estimated in a similar manner from the Rabi oscillation between the two states. The measured results are $(25.4 \pm 1.3)\%$ for $|0\rangle$ and $(51.1 \pm 2.1)\%$ for $|+1\rangle$. The probabilities of $|0\rangle$ and $|-1\rangle$ can be estimated by the Rabi oscillation between the two states. The measured results are $(25.9 \pm 0.8)\%$ for $|0\rangle$ and $(24.7 \pm 1.5)\%$ for $|-1\rangle$. Summarised together, the relative probabilities of $|0\rangle$, $|+1\rangle$ and $|-1\rangle$ can be determined and are shown in inset “a” of Figure 3. The probability values are 25.22% for $|0\rangle$ (yellow sector), 50.44% for $|+1\rangle$ (red sector) and 24.33% for $|-1\rangle$ (green sector). For the output state with the form $\frac{1}{2}|0\rangle + \frac{1}{2}|1\rangle + \frac{1}{\sqrt{2}}e^{i\varphi}|+1\rangle$, the expected values are 25%, 50% and 25%. Based on the magnitude of the deviation of the measurement, the experimental results are consistent with the expected values.

These experimental procedures are repeated with three other states: Φ_2 , Φ_3 and Φ_4 . States with different phases are prepared through adjustments of the manual phase shifter, and the state phases are measured before cloning. The measured results are $128.2^\circ \pm 1.6^\circ$, $-47.7^\circ \pm 1.7^\circ$ and $-138.4^\circ \pm 2^\circ$. The state phase measurement is performed again after the cloning process. The phase values are $124.3^\circ \pm 1.7^\circ$, $-48.3^\circ \pm 3.3^\circ$ and $-140.3^\circ \pm 2.9^\circ$, respectively. The errors are the standard deviation of five measurements, and these results are shown in Figure 3. The phase change values during the cloning process are -3.9° , -0.6° and -1.9° . The phase information is well preserved during the cloning process. The probabilities of states Φ_2 , Φ_3 and Φ_4 are also confirmed by measurements. The relative probabilities of $|0\rangle$, $|+1\rangle$ and $|-1\rangle$ are 23.26%, 52.49% and 24.24% for state Φ_2 (Fig. 4, inset b), 25.7%, 50.05% and 24.25% for state Φ_3 (Fig. 4, inset c) and 24.95%, 49.23% and 25.82% for state Φ_4 (Fig. 4, inset d). All of the results are highly consistent with the expected values.

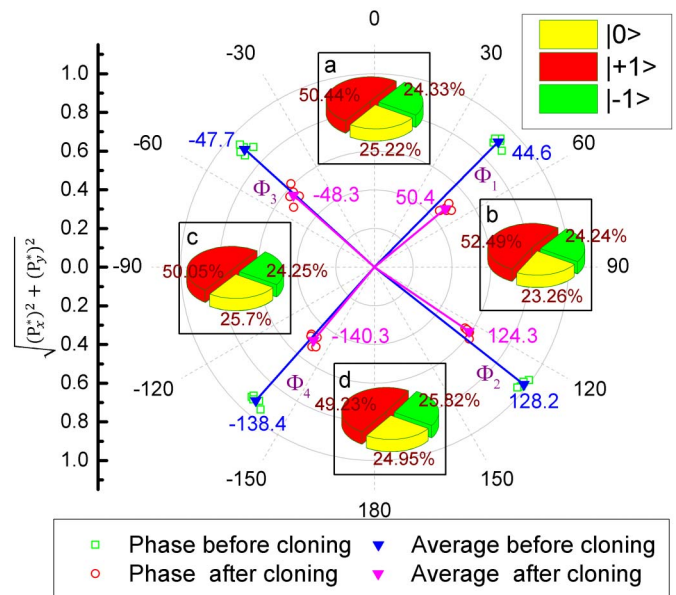


Figure 3 | Measured results for the quantum state phase and relative probability. The scatter points show the experimental data, and the lines with the solid triangles display the averaged values. The blue lines represent the measured phases Φ_1 , Φ_2 , Φ_3 and Φ_4 for four different input states, and the magenta lines show the measured phases after the cloning process. Insets a, b, c and d show the relative probability results after cloning for states Φ_1 , Φ_2 , Φ_3 and Φ_4 , respectively. The yellow sectors show the probability of $|0\rangle$, red shows $|+1\rangle$, and green shows $|-1\rangle$.

Density matrices and fidelities. We can denote the physical output state in the form $\alpha|0\rangle + \beta e^{i\varphi}|+1\rangle + \gamma|-1\rangle$ and $|\alpha|^2 + |\beta|^2 + |\gamma|^2 = 1$, because the relative phase of $|-1\rangle$ is fixed at 0° in all of the experiments. From the results of the state phase and probability measurements, the physical output states and their density matrices can be determined. The matrix elements of states Φ_1 , Φ_2 , Φ_3 and Φ_4 are shown in Figure 4. The diagonal elements have a one-to-one correspondence between the matrix and the columns in the figure. The yellow columns indicate the elements $\rho_{0,0}$, red indicates $\rho_{+1,+1}$, and green indicates $\rho_{-1,-1}$. Because the density matrix is conjugated, the real and imaginary parts of the off-diagonal elements are shown together in Figure 4. The blue columns indicate the real part $(\rho_{0,+1} + \rho_{+1,0})/2$, and the cyan columns indicate the imaginary part $(\rho_{+1,0} - \rho_{0,+1})/2i$. Matrix elements that are not involved in the experiment are shown as grey columns with calculated heights.

Decoding the logic output states from the physical states, we can calculate the fidelities between the input states and their copies after cloning. By tracing out one qubit degree of freedom from the density matrix of the output state after decoding, we obtain the two copies (ρ_1 and ρ_2) of the input state $(|\psi\rangle = (|0\rangle + e^{i\varphi}|1\rangle) / \sqrt{2})$. In measuring the phase of the input state before cloning, we note that the sum of P_x^2 and P_y^2 is less than 1, ($P_z = 0$, see Fig. 2(c) for information about P_x , P_y , P_z). Phase amplitude $(P_x^2 + P_y^2)$ damping occurs during preparation and measurement⁴⁷. We scale $P_x^2 + P_y^2$ to 1 and compensate the results for P_x^2 and P_y^2 after cloning based on the damping rate. For the compensated density matrix ρ^c , the fidelities of the two copies are $F_1^c = \langle \psi | \rho_1^c | \psi \rangle$ and $F_2^c = \langle \psi | \rho_2^c | \psi \rangle$. The calculated results are $F_1^c = 78.5\%$ and $F_2^c = 78.0\%$ for state Φ_1 , $F_1^c = 79.7\%$ and $F_2^c = 80.3\%$ for state Φ_2 , $F_1^c = 84.6\%$ and $F_2^c = 83.0\%$ for state Φ_3 and $F_1^c = 79.0\%$ and $F_2^c = 79.5\%$ for state Φ_4 . The compensated experimental fidelities are 78.3% for state Φ_1 , 80.0% for state Φ_2 , 83.8% for state Φ_3 and 79.2% for state Φ_4 . The average experimental fidelity is 80.3%.

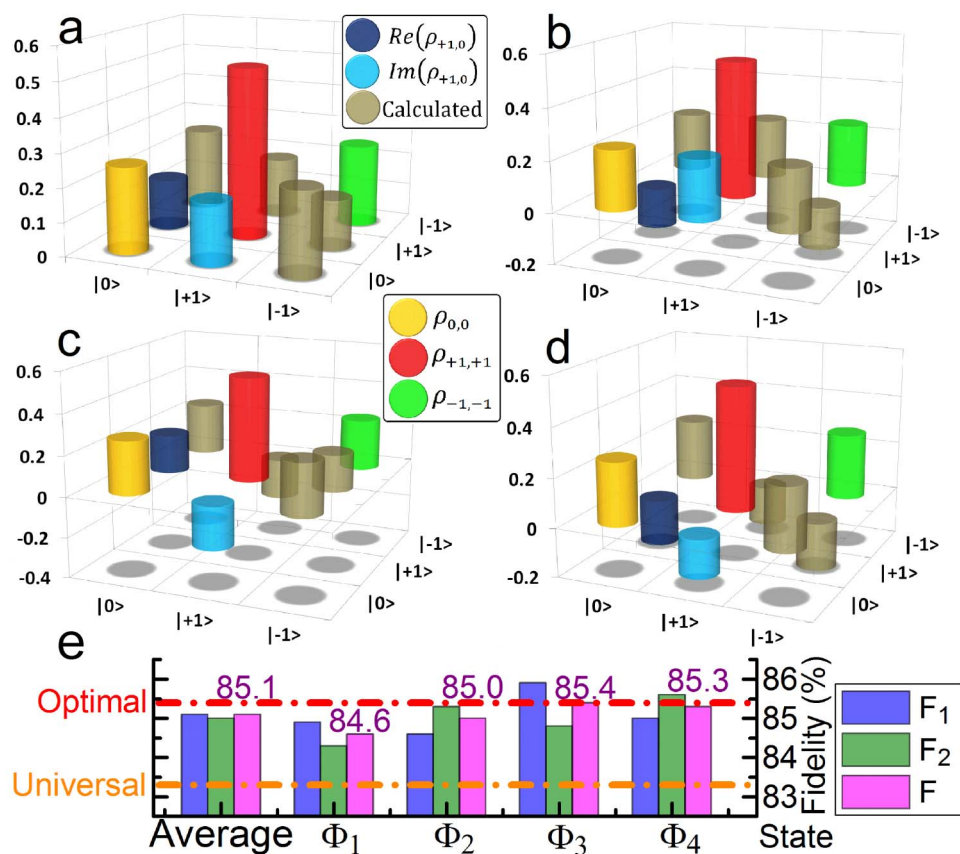


Figure 4 | Results for density matrices and phase cloning fidelity. a, b, c and d illustrate the results for states Φ_1, Φ_2, Φ_3 and Φ_4 , respectively. The yellow columns correspond to the diagonal elements of the density matrix and indicate $\rho_{0,0}$, red indicates $\rho_{+1,+1}$, and green indicates $\rho_{-1,-1}$. The real and imaginary parts of the off-diagonal elements are shown together. The blue columns indicate the real part $(\rho_{0,+1} + \rho_{+1,0})/2$, and the cyan columns indicate the imaginary part $(\rho_{+1,0} - \rho_{0,+1})/2i$. The matrix elements that are not involved are illustrated by grey columns with calculated heights. e. Fidelity results for states Φ_1, Φ_2, Φ_3 and Φ_4 and their average values. The blue and green columns show the fidelities of the two output copies; the averages for these copies are shown with magenta columns. The red dash-dot line represents the expected optimal cloning fidelity, 85.4%, and the orange line displays the universal cloning bound, 83.3%.

The extracted information for the relative probabilities and phase φ is sufficient for phase cloning, so we can calculate the phase fidelity separately. This calculation includes the additional assumption that phase decoherence is negligible in the experiment. If phase damping is ignored, the fidelities of the two output copies are $F_1 = \langle \psi | \rho_1 | \psi \rangle$ and $F_2 = \langle \psi | \rho_2 | \psi \rangle$. The calculated results are $F_1 = 84.9\%$ and $F_2 = 84.3\%$ for state Φ_1 , $F_1 = 84.6\%$ and $F_2 = 85.3\%$ for state Φ_2 , $F_1 = 85.9\%$ and $F_2 = 84.8\%$ for state Φ_3 and $F_1 = 85.0\%$ and $F_2 = 85.6\%$ for state Φ_4 . The phase fidelity results are 84.6% for state Φ_1 , 85.0% for state Φ_2 , 85.4% for state Φ_3 and 85.3% for state Φ_4 . The average phase fidelity, 85.1%, is very close to the theoretical fidelity, 85.4%. These results are shown in Figure 4(e). Thus, phase cloning is successfully implemented in the experiment.

Discussion

In this work, we have demonstrated the first room-temperature implementation of a quantum phase cloning machine with controllable phase in a solid-state system composed of nanodiamond. Nanodiamond has great advantages for future applications; however, its short dephasing time brings new challenges. A carefully calibrated CPW antenna was employed to improve the microwave delivery efficiency. For high-frequency Rabi oscillations, more manipulations can be implemented before decoherence. The microwave phase is precisely controlled in our experiment, and the phase of the quantum state can also be measured with high accuracy. With these

technical developments and preparations, we implemented optimal phase-covariant quantum cloning in our NV nanodiamond system. The experimental results were measured by standard state tomography methods, which are more precisely. The phase information is well preserved during the cloning process. Decoherence from phase damping causes the average experimental fidelity of cloning to be 80.3%, which is 94% of the theoretical value. The fidelity can be improved by a NV with longer dephasing time, faster manipulation and dynamic decoupling techniques^{48–51}. For a phase cloning machine, under the assumption that phase damping in the experiment is negligible, we can use only the relative probabilities and the phase φ to analyse the cloning efficiency of the information. In this way, the calculated phase fidelity is 85.1% on average; this value is close to the theoretical value, 85.4%, and exceeds the universal quantum cloning bound, 83.3%, Figure 4(e). The object states cloned in the experiment can serve as BB84 states in QKDs. Thus, this high-fidelity cloning may play an important role in analysing the security of QKDs. The drawback of this quantum cloning experiment is that the two qubits are encoded in a one-spin system. One possible method for solving this problem is to use both the electron spin and the nuclear spin of the NV centre to encode the two qubits; this encoding is still challenging because the two spins have different coherence times and an accurate readout is difficult. The full control and precise measurement of the quantum phase can be used as a foundation for further applications in QIP. The coherent manipulation and



implementation of the cloning machine in nanodiamond also demonstrate prospects for future scalable quantum information devices.

Methods

Experimental setup. A single NV centre can be found and located with our home-built laser confocal scanning microscope system. The fluorescence emitted from the NV centre is collected with the optical system and is then detected by a single photon counting module connected to the counter terminal of a multifunction data acquisition device (NI USB 6211). To obtain the laser pulses for state polarisation and for readout, an acoustic optical modulator (AOM) modulates a 532-nm continuous-wave laser. The microwave signals are switched by mixer (Minicircuit) pairs for a quick response (nearly real-time) and for a better on-off contrast ratio. The signals that control the mixers are provided by pattern/pulse generators (Agilent 81110A), which run in triggered pulse mode with high time resolution (better than 0.1 ns).

State phase measurement. The Bloch vector for one quantum state can be rotated 90° about the x - or y -axis by a $\pi/2$ microwave pulse with phase X or Y ^{52,53}, [Fig. 2(c)]. The X or Y component (P_x, P_y) of the Bloch vector P is converted to the Z component (P_z), which can be measured through photon counting. Full Rabi oscillation using a microwave with phase X or Y , Rabi X or Rabi Y , is implemented in the experiment. The red circles filled with yellow in Figure 2(d) show the experimental data. Rabi X and Rabi Y are scaled by the standard Rabi oscillation from the pure $|0\rangle$ state (shown by the blue line). In the lower panel of Figure 2(d), the orange arrow indicates the relative distance between the point at the $\pi/2$ position of the fitting line for the Rabi X or Rabi Y data (green) and the line at the middle of the oscillation (dark yellow). Based on the sign (positive or negative), the distance indicates the observation of P_x or P_y in the Bloch sphere representation. After the cloning process, all three energy levels are involved, and the value is denoted as P_x^* or P_y^* . After the measurement of Rabi X and Y , the state phase can be obtained from the value of $\arctan P_y^*/P_x^*$.

State probability measurements. The fluorescence intensity under pulsed laser excitation indicates the probability of $|0\rangle$, which is easily defined by the initial point of the Rabi oscillation. The probability measurement for $|+1\rangle$ or $|-1\rangle$ is indirect, however, and is performed by rotating the Bloch vector and reversing the Z component with a π pulse from MW1 or MW2 [Fig. 2(c)]. Two full Rabi oscillations, Rabi C and Rabi S, are implemented in our experiment. Rabi C with MW2 is used to estimate the probability of $|0\rangle$ and $|-1\rangle$; Rabi S with MW1-M is used to estimate $|0\rangle$ and $|+1\rangle$. Based on prior state phase measurement results, the microwave phase of Rabi S can be adjusted to be similar to that of the prepared state. In the actual experiment, when the phase difference is too large, the fidelity of the measurement process may decrease. In the worse-case scenario, for example, if the two phases are nearly opposite, the fidelity may be less than 80%. As a result, phase adjustment based on prior phase measurement results is beneficial for high measurement fidelity. If scaled by the standard Rabi oscillation of the pure $|0\rangle$ state, the initial height of Rabi C or Rabi S gives the probability of $|0\rangle$, [Fig. 2(d), orange arrow in the upper panel]. The height of the fitting line at π gives the probability of $|-1\rangle$ or $|+1\rangle$, [Fig. 2(d), green arrow in the upper panel]. For the probability of the $|0\rangle$ state, the demonstrated values are the average of the Rabi C and Rabi S measurements.

1. Dieks, D. Communication by electron-paramagnetic-res devices. *Phys. Lett. A* **92**, 271 (1982).
2. Wootters, W. K. & Zurek, W. H. A Single quantum cannot be cloned. *Nature* **299**, 802–803 (1982).
3. Bužek, V. & Hillery, M. Quantum copying: Beyond the no-cloning theorem. *Phys. Rev. A* **54**, 1844–1852 (1996).
4. Bruß, D. *et al.* Optimal universal and state-dependent quantum cloning. *Phys. Rev. A* **57**, 2368–2378 (1998).
5. Gisin, N. & Massar, S. Optimal quantum cloning machines. *Phys. Rev. Lett.* **79**, 2153–2156 (1997).
6. Werner, R. F. Optimal cloning of pure states. *Phys. Rev. A* **58**, 1827–1832 (1998).
7. Cerf, N. J. Pauli cloning of a quantum bit. *Phys. Rev. Lett.* **84**, 4497 (2000).
8. Fan, H., Matsumoto, K. & Wadati, M. Quantum cloning machines of a d-level system. *Phys. Rev. A* **64**, 064301 (2001).
9. Duan, L. M. & Guo, G. C. Probabilistic cloning and identification of linearly independent quantum states. *Phys. Rev. Lett.* **80**, 4999–5002 (1998).
10. Lamas-Linares, A., Simon, C., Howell, J. C. & Bouwmeester, D. Experimental quantum cloning of single photons. *Science* **296**, 712 (2002).
11. Du, J. F. *et al.* Experimental quantum cloning with prior partial information. *Phys. Rev. Lett.* **94**, 040505 (2005).
12. Nagali, E. *et al.* Optimal quantum cloning of orbital angular momentum photon qubits through Hong-Ou-Mandel coalescence. *Nature Photonics* **3**, 720 (2009).
13. Cerf, N. J. & Fiurasek, J. Optical quantum cloning. *Progress in Optics* **49**, ed. Wolf, E. (Elsevier) 455 (2006).
14. Scarani, V., Iblisdir, S., Gisin, N. & Acin, A. Quantum cloning. *Rev. Mod. Phys.* **77**, 1225 (2005).

15. Bennett, C. H. & Brassard, G. in *Proceedings of the IEEE International Conference on Computer, Systems, and Signal Processing, Bangalore, India* (IEEE, New York, 1984), pp 175–179.
16. Bruß, D., Cinchetti, M., D’Ariano, G. M. & Macchiavello, C. Phase-covariant quantum cloning. *Phys. Rev. A* **62**, 012302 (2000).
17. Fan, H., Matsumoto, K., Wang, X. B. & Wadati, M. Quantum cloning machines for equatorial qubits. *Phys. Rev. A* **65**, 012304 (2002).
18. Chen, H., Zhou, X., Suter, D. & Du, J. F. Experimental realization of $1 \rightarrow 2$ asymmetric phase-covariant quantum cloning. *Phys. Rev. A* **75**, 012317 (2007).
19. Pan, X. Y., Liu, G. Q., Yang, L. L. & Fan, H. Solid-state optimal phase-covariant quantum cloning machine. *Appl. Phys. Lett.* **99**, 051113 (2011).
20. Gruber, A. *et al.* Scanning confocal optical microscopy and magnetic resonance on single defect centers. *Science* **276**, 2012 (1997).
21. Neumann, P. *et al.* Multipartite entanglement among single spins in diamond. *Science* **320**, 1326 (2008).
22. Jelezko, F. *et al.* Observation of coherent oscillation of a single nuclear spin and realization of a two-qubit conditional quantum gate. *Phys. Rev. Lett.* **93**, 130501 (2004).
23. Epstein, R. J., Mendoza, F. M., Kato, Y. K. & Awschalom, D. D. Anisotropic interactions of a single spin and dark-spin spectroscopy in diamond. *Nature Physics* **1**, 94 (2005).
24. Gaebl, T. *et al.* Room-temperature coherent coupling of single spins in diamond. *Nature Physics* **2**, 408 (2006).
25. Childress, L. *et al.* Coherent dynamics of coupled electron and nuclear spin qubits in diamond. *Science* **314**, 281 (2006).
26. Jiang, L. *et al.* Repetitive readout of a single electronic spin via quantum logic with nuclear spin ancillae. *Science* **326** (2009)
27. Maze, J. R. *et al.* Nanoscale magnetic sensing with an individual electronic spin in diamond. *Nature* **455**, 644 (2008).
28. Taylor, J. M. *et al.* High-sensitivity diamond magnetometer with nanoscale resolution. *Nature Physics* **4**, 810 (2008)
29. Shi, F. *et al.* Room-temperature implementation of the Deutsch-Jozsa algorithm with a single electronic spin in diamond. *Phys. Rev. Lett.* **105**, 040504 (2010).
30. Togan, E. *et al.* Quantum entanglement between an optical photon and a solid-state spin qubit. *Nature* **466**, 730 (2010).
31. Neumann, P. *et al.* Quantum register based on coupled electron spins in a room-temperature solid. *Nature Physics* **6**, 249 (2010).
32. Gurudev Dutt, M. V. *et al.* Quantum register based on individual electronic and nuclear spin qubits in diamond. *Science* **316**, 1312 (2007).
33. Toyli, D. M. *et al.* Chip-scale nanofabrication of single spins and spin arrays in diamond. *Nano Letters* **10**, 3168 (2010).
34. Balasubramanian, G. *et al.* Ultralong spin coherence time in isotopically engineered diamond. *Nature Materials* **8**, 383 (2009).
35. Beveratos, A. Room temperature stable single-photon source. *Eur. Phys. J. D.* **18**, 191–196 (2002).
36. Huck, A., Kumar, S., Shakoor, A. & Andersen, U. L. Controlled coupling of a single nitrogen-vacancy center to a silver nanowire. *Phys. Rev. Lett.* **106**, 096801 (2011).
37. Andreas Schell, W. *et al.* Single defect centers in diamond nanocrystals as quantum probes for plasmonic nanostructures. *Opt. Express* **19**, 7914–7920 (2011).
38. Englund, D. *et al.* Deterministic coupling of a single nitrogen vacancy center to a photonic crystal cavity. *Nano Lett.* **10**, 3922C3926 (2010).
39. Barclay, P. E., Fu, K. M., Santori, C. & Beausoleil, R. G. Hybrid photonic crystal cavity and waveguide for coupling to diamond NV-centers. *Opt. Express* **17**, 9588C9601 (2009).
40. Fu, K. M. C. *et al.* Coupling of nitrogen-vacancy centers in diamond to a GaP waveguide. *Appl. Phys. Lett.* **93**, 203107 (2008).
41. Park, Y. S., Cook, A. K. & Wang, H. L. Cavity QED with diamond nanocrystals and silica microspheres. *Nano Lett.* **6**, 2075C2079 (2006).
42. Ampem-Lassen, E. *et al.* Nano-manipulation of diamond-based single photon sources. *Opt. Express* **17**, 9588–9601 (2011).
43. Balasubramanian, G. *et al.* Nanoscale imaging magnetometry with diamond spins under ambient conditions. *Nature* **455**, 648 (2008).
44. Schietinger, S. *et al.* Plasmon-enhanced single photon emission from a nanoassembled metaldiamond hybrid structure at room temperature. *Nano Lett.* **9**, 1694 (2009).
45. Igor, A. *et al.* Diamond photonics. *Nature Photonics* **5**, 397–405 (2011).
46. Laraoui, A., Hodges, J. S. & Meriles, C. A. Nitrogen-vacancy-assisted magnetometry of paramagnetic centers in an individual diamond nanocrystal. *Nano Lett.* **12**, 3477–3482 (2012).
47. Matthias Steffen *et al.* State Tomography of Capacitively Shunted Phase Qubits with High Fidelity. *Phys. Rev. Lett.* **97**, 050502 (2006).
48. Viola, L., Knill, E. & Lloyd, S. Dynamical decoupling of open quantum systems. *Phys. Rev. Lett.* **82**, 2417 (1999).
49. Yao, W., Liu, R. B. & Sham, L. J. Restoring coherence lost to a slow interacting mesoscopic spin bath. *Phys. Rev. Lett.* **98**, 077602 (2007).
50. Du, J. F. *et al.* Preserving electron spin coherence in solids by optimal dynamical decoupling. *Nature* **461**, 1265 (2009).
51. Naydenov, B. *et al.* Dynamical Decoupling of a single electron spin at room temperature. *Phys. Rev. B* **83**, 081201 (2011).



52. Bianchetti, R. *et al.* Control and Tomography of a Three Level Superconducting Artificial Atom. *Phys. Rev. Lett.* **105**, 223601 (2010).
53. Thew, R. T., Nemoto, K., White, A. G. & Munro, W. J. Qudit quantum-state tomography. *Phys. Rev. A* **66**, 012303 (2002).

Acknowledgements

This work was supported by “973” programs (2009CB929103, 2010CB922904), NSFC grants (11175248, 10974251) and grants from CAS.

Author contributions

X.-Y.P. and H.F. designed the experiment. X.-Y.P. directed the experiment, and H.F. was responsible for the theory. Y.-C.C., G.-Q.L., D.-Q.L. and X.-Y.P. performed the experiment.

Y.-C.C., G.-Q.L., X.-Y.P. and H.F. analysed the data, and Y.-C.C., X.-Y.P. and H.F. wrote the paper.

Additional information

Competing financial interests: The authors declare no competing financial interests.

License: This work is licensed under a Creative Commons Attribution-NonCommercial-NoDerivs 3.0 Unported License. To view a copy of this license, visit <http://creativecommons.org/licenses/by-nc-nd/3.0/>

How to cite this article: Chang, Y., Liu, G., Liu, D., Fan, H. & Pan, X. Room-Temperature Quantum Cloning Machine with Full Coherent Phase Control in Nanodiamond. *Sci. Rep.* **3**, 1498; DOI:10.1038/srep01498 (2013).